



LAWRENCE
LIVERMORE
NATIONAL
LABORATORY

Spatial and Temporal Characterization of Femtosecond Pulses at High-Numerical Aperture Using Collinear, Background-Free, Third-Harmonic Autocorrelation

D. N. Fittinghoff, J. Aus der Au, and J. A. Squier

August 13, 2004

For submission to Optics Communications

Disclaimer

This document was prepared as an account of work sponsored by an agency of the United States Government. Neither the United States Government nor the University of California nor any of their employees, makes any warranty, express or implied, or assumes any legal liability or responsibility for the accuracy, completeness, or usefulness of any information, apparatus, product, or process disclosed, or represents that its use would not infringe privately owned rights. Reference herein to any specific commercial product, process, or service by trade name, trademark, manufacturer, or otherwise, does not necessarily constitute or imply its endorsement, recommendation, or favoring by the United States Government or the University of California. The views and opinions of authors expressed herein do not necessarily state or reflect those of the United States Government or the University of California, and shall not be used for advertising or product endorsement purposes.

Spatial and temporal characterization of femtosecond pulses at high-numerical aperture using collinear, background-free, third-harmonic autocorrelation

David N. Fittinghoff
*Lawrence Livermore National Laboratory
L-472, Livermore, CA 94551-0808 USA
fittinghoff1@llnl.gov*

Jürg Aus der Au
Spectra-Physics, Mountain View, Ca

Jeff Squier
*Department of Physics, Colorado School of Mines
Golden, CO 80401 USA*

Abstract

We show that a simple plane wave analysis can be used even under tight focusing conditions to predict the dependence of third-harmonic generation on the polarization state of the incident beam. Exploiting this fact, we then show that circularly polarized beams may be used to spatially characterize the beam focus and temporally characterize ultrashort pulses in high numerical aperture systems by experimentally demonstrating, for the first time, novel collinear, background-free, third-harmonic intensity autocorrelations in time and space in a high numerical aperture microscope. We also discuss the possibility of using third harmonic generation with circularly polarized beams for background-free collinear frequency resolved optical gating.

One of the most intriguing applications for ultrashort pulse lasers is the generation of image contrast through the efficient excitation of an optical nonlinearity. Probably the most prevalent nonlinear imaging technique is multiphoton absorption fluorescence microscopy[1], which relies on multiphoton absorption fluorescence of either endogenous species or specific fluorophores attached as a label to a target body. The high intensity dependence of the absorption localizes the subsequent fluorescence emission to the focal volume making it possible to generate cross sectional images of the specimen similar to those obtained with traditional laser fluorescent confocal imaging techniques. The absolute value in using ultrashort pulses for this application is that longer excitation wavelengths are used, which allows increased penetration in most tissues, and that out-of-focal plane bleaching is eliminated. (We note that it has recently been demonstrated that bleaching within the focal plane could in fact occur at a substantially higher rate [2].)

We undertook this work to further our understanding of another nonlinear mechanism, third-harmonic generation (THG), which can be used to provide cross sectional images of living biological systems in much the same manner as multiphoton absorption fluorescence microscopy. While Ward and New described the THG produced by focusing Gaussian beams in their seminal work in the 1960's [3], it was not until Tsang[4] demonstrated that he could produce substantial optical signal consisting of odd harmonics by focusing exclusively at an interface under tight focusing conditions (high numerical aperture) that its' use for imaging of fibers and biological specimens[5, 6] and for noncollinear frequency-resolved optical gating measurements and interferometric autocorrelations[7, 8] arose. In this work, we investigate the polarization dependence of

the THG process under tight focusing conditions. Specifically, we show that, even under tight focusing conditions, a simple plane wave analysis of the signal can be used to predict the polarization dependence of third-harmonic generated in a focus as a function of the polarization state of the incident beam. This is significant in that ellipticity is an additional parameter that might be exploited to provide image contrast, and these measurements enable a quantitative measure of these image intensities in a very simple way. Exploiting the fact that we may use the plane wave analysis, we then characterize the spatial focus of high numerical aperture (NA) systems and make novel collinear, background-free, third-harmonic intensity autocorrelation of the pulse at the focus. This is significant because prior to this work there has been no single tool that provided background free spatio-temporal characterization of focal volumes such as those used in high-resolution microscopy. We also discuss the possibility of using third harmonic generation with circularly polarized beams for background-free collinear frequency resolved optical gating.

All the measurements performed in this article use the nonlinear medium most convenient for the microscopist: a glass coverslip. Indeed, one of the greatest uses of this work is that most of the components that are necessary for spatio-temporal characterization are already in place. In multiphoton microscopes, the third harmonic signal is necessarily present and quite strong at the ubiquitous glass coverslip interface. Finally, as we demonstrate here, a straightforward plane-wave analysis is all that is necessary to understand and analyze this signal, even under tight focusing conditions.

For convenience, this Article is arranged into several sections. The next three sections present the core results of the Article. In Section I, we present a simple plane

wave analysis to calculate the polarization state of the output THG signal explicitly as a function of input ellipticity and present experimental measurements of the dependence of THG on the input polarization. These measurements show that only the straightforward, plane wave calculations are necessary to predict the polarization dependence of the measured THG. In Section II, we use this analysis to determine the output THG signal for overlapping Gaussian beams and demonstrate the use of the THG produced by oppositely circularly polarized beams for characterization of the lateral spatial profile of a 0.65 NA focus. The THG produced at an interface by the focused beam with a linear polarization is also used to characterize the axial spatial profile of the focus. Then in Section III, we show that oppositely circularly polarized beams may also be used to produce background-free THG autocorrelations of the ultrashort pulses at such a focus.

In Section IV, we show that circularly polarized beams could potentially be used to perform collinear, background-free frequency-resolved optical gating (FROG) measurements of the temporal pulse amplitude and phase of an ultrashort laser pulse.

Finally, in Section V, we summarize our results and conclusions. Section VI is an Appendix that presents calculations of the derivatives required for performing a generalized projections phase retrieval of the amplitude and phase of an ultrashort pulse from two of the FROG methods discussed in Section IV.

I. Ellipticity dependence of THG generation

The problem of determining the polarization of the third-harmonic generated by an elliptically polarized, tightly focused Gaussian beam has not, to our knowledge, been solved. Bey and Rabin[9] have, however, solved the problem for elliptically polarized

plane waves propagating along the optic axis (z-direction) of crystals of point symmetry 32 that are optically active. The form of their results are equally applicable in form for an isotropic medium, and this is the paper quoted by Ward and New[3] when they state that a circularly polarized fundamental does not generate harmonic for an isotropic nonlinear medium. The actual results that they obtain for the left-handed and right-handed third harmonic amplitudes, $E_{3\omega}^{\pm}(l)$, generated by an electric field, $E_{\omega}(z)$, at the fundamental frequency, ω , in a medium of thickness l are

$$E_{3\omega}^{\pm}(l) = \frac{27\pi C_{1122}}{4k_3} \left(\frac{\omega}{c}\right)^2 \left(E_{\omega}^{\pm}(0)\right)^2 E_{\omega}^{\mp}(0) \times \left\{ \frac{1 - e^{-i[(\Delta k)_{THG} \pm (\Delta \alpha)_{THG}]l}}{(\Delta k)_{THG} \pm (\Delta \alpha)_{THG}} \right\} \quad (1)$$

Here + indicates the left-handed circular components and – indicates the right-handed circular components, and the entrance face of the material is assumed to be at $z = 0$. C_{1122} is the non-vanishing component of the fourth-rank electric susceptibility tensor, and c is the speed of light in vacuum. The wave vector mismatch and mismatch of the specific rotation of the polarization are, respectively,

$$\begin{aligned} (\Delta k)_{THG} &= k_3 - 3k_1, \\ (\Delta \alpha)_{THG} &= \alpha_3 - \alpha_1. \end{aligned} \quad (2)$$

where $\alpha_i = (k_i^+ - k_i^-)/2 = \omega_i f_i / 2c$, where f_i is a pseudo scalar measuring the magnitude of the specific rotation at the frequency, and k_1 and k_3 are the wave vectors of the fundamental and third-harmonic, respectively.

Explicit Calculation of the THG Polarization State

Since using the circularly polarized components are often more useful than the linear components when dealing with elliptically polarized beams we will now use this simple plane wave analysis and calculate the polarization state of the output light explicitly. We add the components vectorially

$$\mathbf{E}_{3\omega}(l) = \mathbf{E}_{3\omega}^+(l) + \mathbf{E}_{3\omega}^-(l). \quad (3)$$

In this calculation we are not concerned that the medium is optically active, and therefore neglect this rotation. Putting in the amplitudes explicitly and dropping the common factors then gives

$$\begin{aligned} \mathbf{E}_{3\omega}(l) &\propto \begin{bmatrix} 1 \\ -i \end{bmatrix} \left(\mathbf{E}_{\omega}^+(0) \right)^2 \mathbf{E}_{\omega}^-(0) + \begin{bmatrix} 1 \\ i \end{bmatrix} \left(\mathbf{E}_{\omega}^-(0) \right)^2 \mathbf{E}_{\omega}^+(0) \\ &\propto \mathbf{E}_{\omega}^+(0) \mathbf{E}_{\omega}^-(0) \begin{bmatrix} \mathbf{E}_{\omega}^+(0) + \mathbf{E}_{\omega}^-(0) \\ i(\mathbf{E}_{\omega}^+(0) - \mathbf{E}_{\omega}^-(0)) \end{bmatrix} \end{aligned} \quad (4)$$

We note that, alternatively, the polarization state may be described by an ellipticity angle, ε , and the rotation of the polarization ellipse, θ , as shown in Figure 1. The ellipticity angle may be written

$$\varepsilon = \frac{1}{2} \sin^{-1} \left(\frac{2 \operatorname{Im}(\chi)}{1 + |\chi|^2} \right). \quad (5)$$

where

$$\chi \equiv \frac{E_y}{E_x} = i \frac{E_{\omega}^{+}(0) - E_{\omega}^{-}(0)}{E_{\omega}^{+}(0) + E_{\omega}^{-}(0)} \quad (6)$$

The rotation of the polarization ellipse is then

$$\theta = \tan^{-1} \left(\frac{\text{Im}(\chi) - \tan(\varepsilon)}{\tan(\varepsilon) \text{Re}(\chi)} \right). \quad (7)$$

By explicitly substituting the form of χ into the equation for the ellipticity angle, it is possible to show that the ellipticity of the generated third-harmonic is

$$\varepsilon_{3\omega} = \frac{1}{2} \sin^{-1} \left(\frac{(E_{\omega}^{+}(0))^2 - (E_{\omega}^{-}(0))^2}{(E_{\omega}^{+}(0))^2 + (E_{\omega}^{-}(0))^2} \right). \quad (8)$$

We can see by inspection that the ellipticity angle is only zero when the left and right circularly polarized amplitudes have equal square magnitudes, or in other words for a linearly polarized input beam. Thus the third-harmonic beam that is generated is linearly polarized only for a linearly polarized input and is elliptically polarized otherwise.

What then does that ellipticity of the third-harmonic signal look like as the ellipticity of the input fundamental beam changes? It is straightforward to calculate the variation of the THG amplitude as a function of the amplitudes $E_{\omega}^{+}(0)$ and $E_{\omega}^{-}(0)$. In

Figures 2 and 3, we hold the amplitude $E_{\omega}^{+}(0)$ constant and vary $E_{\omega}^{-}(0)$ from zero to $E_{\omega}^{+}(0)$ while plotting the x- and y-components of the THG field, and the magnitude and the ellipticity angle, respectively. As one would expect, the figures show that the emitted field is highly elliptical for small $E_{\omega}^{-}(0)$ where the fundamental beam is nearly circularly polarized but becomes linear as the left and right circular components become equal and the total fundamental field becomes linear. The magnitude of the THG also increases as the total field becomes linear. The rotation of the polarization ellipse is always zero by definition.

Experimental measurements of the THG ellipticity versus input polarization

The analysis above is valid for a plane wave, but is it a valid representation of the variation of the THG signal with input polarization in a high NA microscope where the beam is tightly focused? To answer this question, we measured the THG signal as a function of the input polarization in a high NA microscope.

For this measurement, we used our entirely home-built harmonic microscope, which is powered by a diode-pumped Nd:glass (phosphate) laser. This laser is based on the work of Kopf et al.[10] with the following specifications. The average output power is 100 mW, the pulse duration is 150 fs, and the repetition rate is 100 MHz. In a slight design simplification, we have achieved this performance using only a single pump diode. The glass rod is mounted in a copper heat sink that is cooled only by the ambient air. A schematic of the laser design is shown in Figure 4.

The output of the laser passes through an autocorrelator before being directed through the scan mirrors and into the microscope. The polarization state of each of the beams can be independently controlled. One arm of the autocorrelator can be delayed in

time with respect to the other through an automated axial displacement, as well as spatially shifted by an automated angular displacement. This enables both spatial and temporal autocorrelations to be performed at the focus of the microscope.

The microscope also features dual signal detection (Figure 5). Optical signals at both the second and third harmonic are captured in the forward direction. In the back direction, multiphoton absorption fluorescence signals are measured. In this way images created through the three different techniques are fully registered with respect to each other. In general the collected radiation is detected with photomultipliers (Hamamatsu model R5600U-3) making it possible to scan through scattering and nonscattering samples. (For nonscattering samples the PMT's are often replaced with cameras, Hamamatsu model C5985). The PMT signal is sent through a simple current-to-voltage converter that is sampled by an analog-to-digital board.

Detection, and scanning are controlled through a LabView interface that we developed specifically for this imaging system. The beam is rastered by two General Scanning galvanometric mirrors (model VM2015) that provide lateral image capability, while the specimen is scanned axially using an encoded stepper motor stage from AF Optical for complete three-dimensional sectioning. The scanned beam is appropriately relayed to the objective by the lens series shown in Figure 5. One of the concerns when working with ultrashort pulses and nonlinear imaging techniques is the dispersion introduced by intermediate relay optics. We have calculated the dispersion for this system and find that it is 180 fs^2 at 800 nm and 86 fs^2 at 1054 nm. In addition, we have calculated this dispersion as a function of scan angle. If we consider in this context the dispersion only at 800 nm (which is the worse case scenario) we find the dispersion changes by ~ 10

fs² for an angular shift of 3 degrees. This means a pulse 30 fs in duration will only broaden by 2 fs at the extremes of the scan. Thus, pulse dispersion as a function of angle through the scan optics is basically negligible for most applications. This is an especially important consideration for the spatial correlation measurements, and enables us to reliably treat the data as an autocorrelation as opposed to cross correlation.

Rather than vary the amplitude of one of the beams as was done theoretically to obtain the results shown in Figures 2 and 3, we chose to vary the polarizations. In our experiment, we placed a motorized $\lambda/2$ -wave plate and a stationary $\lambda/4$ -wave plate in the beam path to control the polarization of the input fundamental beam.

In the following, we derive the function used to fit our experimental data:

(1) Jones matrix for $\lambda/2$ -waveplate:

$$\mathbf{M}_1 = \begin{pmatrix} 1 & 0 \\ 0 & -1 \end{pmatrix} \quad (9)$$

(2) Jones matrix for $\lambda/4$ -wave plate:

$$\mathbf{M}_2(\beta) = \begin{pmatrix} 1 & 0 \\ 0 & e^{i\pi\beta} \end{pmatrix} \quad (10)$$

with β close to 0.5 (used as fit parameter $w[0]$)

(3) Rotation matrix:

$$\mathbf{R}(\theta) = \begin{pmatrix} \cos\theta & \sin\theta \\ -\sin\theta & \cos\theta \end{pmatrix} \quad (11)$$

Rotation of the half-wave plate gives us an arbitrarily orientated linearly polarized beam:

$$\begin{pmatrix} a \\ b \end{pmatrix} = (\mathbf{R}(-\theta) \cdot \mathbf{M}_1 \cdot \mathbf{R}(\theta)) \cdot \begin{pmatrix} 1 \\ 0 \end{pmatrix} = \begin{pmatrix} \cos^2(\theta) - \sin^2(\theta) \\ 2\sin(\theta)\cos(\theta) \end{pmatrix} \quad (12)$$

By putting the resulting beam through a $\lambda/4$ wave plate, we end up with:

$$\mathbf{E}_\omega \propto \mathbf{M}_2(\beta) \cdot \begin{pmatrix} a \\ b \end{pmatrix} = \begin{pmatrix} a \\ b \exp(i\pi\beta) \end{pmatrix} \quad (13)$$

On the detection side, we had a polarizer right in front of our photodetector. This

polarizer can be described by $\mathbf{P} = \begin{pmatrix} \cos(p\pi) \\ \sin(p\pi) \end{pmatrix}$. Therefore, the photodetector will see the

square of the following field:

$$\mathbf{E}_{3\omega} \propto \mathbf{E}_\omega \mathbf{E}_\omega \mathbf{E}_\omega \cdot \mathbf{P} = (a^2 + b^2 \exp(i\pi\beta)) \begin{pmatrix} a \\ b \exp(i\pi\beta) \end{pmatrix} \cdot \begin{pmatrix} \cos(p\pi) \\ \sin(p\pi) \end{pmatrix} \quad (14)$$

$$\mathbf{E}_{3\omega} \propto (a^2 + b^2 \exp(i\pi\beta))(a \cos(p\pi) + b \exp(i\pi\beta) \sin(p\pi))$$

leading finally to the following expression for the measured THG intensity:

$$\begin{aligned} I_{3\omega} &\propto \mathbf{E}_{3\omega} \cdot \mathbf{E}_{3\omega}^* \\ &\propto (a^4 + b^4 + 2a^2b^2 \cos(\pi\beta)) \\ &\quad \times (a^2 \cos^2(p\pi) + b^2 \sin^2(p\pi) + 2ab \cos(p\pi) \sin(p\pi) \cos(\pi\beta)) \end{aligned} \quad (15)$$

Fit Function

Equation (15) was used to fit our data. More precisely, we set the polarizer such that $p = 1/2$, and used the following function:

$$I_{fit} = A(\varphi)^6 w[2] b^2 (a^4 + b^4 + 2a^2 b^2 \cos(\pi\beta)) \quad (16)$$

where a and b are defined through (see also Equation (12))

$$\begin{aligned} a &= \cos^2\{\pi(\varphi - w[4])w[3]\} - \sin^2\{\pi(\varphi - w[4])w[3]\} \\ b &= 2 \sin\{\pi(\varphi - w[4])w[3]\} \cos\{\pi(\varphi - w[4])w[3]\} \end{aligned} \quad (17)$$

and the amplitude $A(\varphi)$ (=variation of the fundamental power through the rotation of the half-wave plate) was measured in the experimental setup. The angle φ is the rotation angle of the half-wave plate and corresponds to the plotted angle in our graphs.

We have a total of five fit-parameters; four of the five are shown above (and below) and labeled with $w[0]$ through $w[4]$. The sixth parameter $w[5]$ is buried within the amplitude A . The parameters $w[0]$ through $w[4]$ have the following meanings:

$w[0] = \beta$	Ellipticity	This parameter describes how good our $\lambda/4$ -wave plate actually is; should be close to 0.5 and the same for both polarizations(see e.g. graphs for NA 0.65, Figure 6: $w[0]=0.55$)
$w[2]$	Amplitude	used to adjust overall amplitude
$w[3]$	Scaling	should be close to 1

$w[4]$ Offset used to adjust angle (should be the same within an experiment, see e.g. graphs for NA 0.65, Figure 6: $w[4]=0.15$)

The measured and fit results are shown in Figures 6 and 7. Figure 6 is measured at a NA of 0.65, and Figure 7 is measured at an NA of 1.4. This result shows that a plane wave analysis of the polarization state produced during THG is still valid even under the strong focusing produced by a high-NA objective. We can now use this analysis as the basis for several measurements of the spatial and temporal properties of focusing beams in a microscope.

II. The polarization state of the THG signal generated by two overlapping Gaussian beams of opposite circular polarization.

When imaging with a high-NA objective, it is important to be able to look at the focal intensity produced at the focus as this determines the resolution of the system. To date, collinear, interferometric measurements that rely on two-photon absorption fluorescence are the primary method for making these measurements [11].

Here we would like to demonstrate the use of THG for these measurements. Our measurements will show that the results of Ward and New, which described THG by a focused linearly polarized Gaussian beam, can be used to describe the axial dependence for circularly polarized beams as well. We will also show that a plane wave description of the THG by two overlapping Gaussians of opposite circular polarizations may be used to accurately describe a spatial THG correlation measurement of the lateral beam focal spot.

Now, let us consider the electric field polarization of the total electric field generated by two overlapping Gaussian beams propagating in the same direction under the assumption that we can use the plane wave analysis to describe the polarization state.

The fundamental field of a single Gaussian beam of arbitrary elliptical polarization

A single Gaussian beam of wavelength, λ , polarized in the i -direction (normal to the z -direction) and propagating in the z -direction in an isotropic, nonmagnetic medium of index, n , may be written as

$$\mathbf{E}_i(\mathbf{r}, t) = \mathbf{e}_i \left\{ \hat{\mathbf{E}}_i(\mathbf{r}, t) e^{i(kz - \omega t)} e^{i\delta_i} + c.c. \right\}. \quad (18)$$

Here ω is the angular frequency of the beam, $k = 2\pi n(\omega)/\lambda$ and δ_i is an absolute phase. \mathbf{e}_i is the unit vector in the direction i . The complex slowly varying amplitude of the beam is given by

$$\hat{\mathbf{E}}_i(\mathbf{r}) = \hat{\eta} A_i e^{-\hat{\eta} k r^2 / 2 z_R}. \quad (19)$$

Here A_i is the amplitude and can be slowly varying in time, z_R is the Rayleigh length of the beam, and

$$\hat{\eta}(z) = \frac{1}{1 + i z / z_R}. \quad (20)$$

Note that we use a caret to indicate a complex quantity. We can generate a beam with an arbitrary polarization by combining two beams polarized in the x and y directions.

$$\begin{aligned}\mathbf{E}(\mathbf{r}, t) &= \left\{ \mathbf{e}_x \hat{\eta} A_x e^{-\hat{\eta} k r^2 / 2 z_R} e^{i \delta_x} + \mathbf{e}_y \hat{\eta} A_y e^{-\hat{\eta} k r^2 / 2 z_R} e^{i \delta_y} \right\} e^{i(kz - \omega t)} + c.c \\ &= \left\{ \mathbf{e}_x A_x e^{i \delta_x} + \mathbf{e}_y A_y e^{i \delta_y} \right\} \hat{\eta} e^{-\hat{\eta} k r^2 / 2 z_R} e^{i(kz - \omega t)} + c.c\end{aligned}\quad (21)$$

Explicitly stating the x and y dependence,

$$\mathbf{E}(x, y, z, t) = \left\{ \mathbf{e}_x A_x e^{i \delta_x} + \mathbf{e}_y A_y e^{i \delta_y} \right\} \hat{\eta} e^{-\hat{\eta} k (x^2 + y^2) / 2 z_R} e^{i(kz - \omega t)} + c.c. \quad (22)$$

Identical elliptically polarized Gaussian beams offset in x by $\pm x_0$

Now let us look at the effect of overlapping two beams offset from each other in one lateral dimension. To achieve this, we consider two beams and offset beam #1 from the origin by a distance x_0 and beam #2 by a distance $-x_0$ where $x_0 \geq 0$. Assuming that the beams have the same Rayleigh length, the beams are then

$$\mathbf{E}_1(x, y, z, t) = \left\{ \mathbf{e}_x A_{x1} e^{i \delta_{x1}} + \mathbf{e}_y A_{y1} e^{i \delta_{y1}} \right\} \hat{\eta} e^{-\hat{\eta} k ((x-x_0)^2 + y^2) / 2 z_R} e^{i(kz - \omega t)} + c.c \quad (23)$$

and

$$\mathbf{E}_2(x, y, z, t) = \left\{ \mathbf{e}_x A_{x2} e^{i \delta_{x2}} + \mathbf{e}_y A_{y2} e^{i \delta_{y2}} \right\} \hat{\eta} e^{-\hat{\eta} k ((x+x_0)^2 + y^2) / 2 z_R} e^{i(kz - \omega t)} + c.c \quad (24)$$

The total separation is thus $2x_0$, and for arbitrary polarizations of the beams the total electric field is

$$\mathbf{E}_{Total}(x, y, z, t) = \mathbf{E}_1(x, y, z, t) + \mathbf{E}_2(x, y, z, t). \quad (25)$$

Two overlapping Gaussian beams of opposite circular polarizations

Now let us assume that $\mathbf{E}_1(x, y, z, t)$ and $\mathbf{E}_2(x, y, z, t)$ have equal amplitudes and that $\mathbf{E}_1(x, y, z, t)$ is left circularly polarized while $\mathbf{E}_2(x, y, z, t)$ is right circularly polarized. Using the convention that a photon with right circular polarization has a positive angular momentum along the direction of propagation, this means that

$$A_{x1} = A_{x2} = A_{y1} = A_{y2} = A,$$

$$e^{i\delta_{x1}} = e^{i\delta_{x2}} = 1, \text{ and}$$

$$e^{i\delta_{y1}} = -e^{i\delta_{y2}} = i.$$

Ignoring the time dependence, the total electric field may be written as

$$\hat{\mathbf{E}}_{Total}(x, y, z) = \left[\left\{ \mathbf{e}_x + i\mathbf{e}_y \right\} e^{-\eta k(x-x_0)^2/2z_R} + \left\{ \mathbf{e}_x - i\mathbf{e}_y \right\} e^{-\eta k(x+x_0)^2/2z_R} \right] \times A \hat{\eta} e^{-\eta k y^2/2z_R} \quad (26)$$

After some manipulation, one may show that

$$\hat{\mathbf{E}}_{Total}(x, y, z) = \left[\mathbf{e}_x \cosh(\hat{\eta} k x x_0 / z_R) + i\mathbf{e}_y \sinh(\hat{\eta} k x x_0 / z_R) \right] \times 2A \hat{\eta} e^{-\eta k(x^2+y^2)/2z_R} e^{-\eta k x_0^2/2z_R} \quad (27)$$

Spatial THG correlations for two beams of opposite circular polarization

Let us now consider the fundamental field of two Gaussian beams that have opposite circular polarizations and that are offset by $\pm x_0$ in the x-y plane. In the x-y plane, $z = 0$, and $\hat{\eta} = 1$. Thus, Equation 27 becomes

$$\hat{\mathbf{E}}_{Total}(x, y, z = 0) = \left[\mathbf{e}_x \cosh(kxx_0/z_R) + i\mathbf{e}_y \sinh(kxx_0/z_R) \right] \times 2Ae^{-k(x^2+y^2)/2z_R} e^{-kx_0^2/2z_R} \quad (28)$$

If we also assume that essentially all of the THG generated is generated at the $z=0$ plane, which is reasonable for high NA (i.e., as the NA increases the axial volume which contributes to the signal decreases, the tighter focusing conditions result in restricting the THG signal production ever closer to the interface), we can use the plane wave approximation from Equation 4

$$\mathbf{E}_{3\omega}(0) \propto E_{\omega}^{+}(0)E_{\omega}^{-}(0) \begin{bmatrix} E_{\omega}^{+}(0) + E_{\omega}^{-}(0) \\ i(E_{\omega}^{+}(0) - E_{\omega}^{-}(0)) \end{bmatrix} \quad (29)$$

A straightforward way to decompose the electric field into left and right circularly polarized components is to use the matrix representations for left and right circular polarizers. Suppressing the time and delay dependence for clarity

$$\mathbf{E}^+ = \mathbf{M}^+ \cdot \mathbf{E} = \frac{1}{2} \begin{bmatrix} 1 & i \\ -i & 1 \end{bmatrix} \cdot \begin{bmatrix} E_x \\ E_y \end{bmatrix} = \frac{1}{2} \begin{bmatrix} E_x + iE_y \\ -iE_x + E_y \end{bmatrix} \quad (30)$$

and

$$\mathbf{E}^- = \mathbf{M}^- \cdot \mathbf{E} = \frac{1}{2} \begin{bmatrix} 1 & -i \\ i & 1 \end{bmatrix} \cdot \begin{bmatrix} E_x \\ E_y \end{bmatrix} = \frac{1}{2} \begin{bmatrix} E_x - iE_y \\ iE_x + E_y \end{bmatrix} \quad (31)$$

where the plus sign indicates right circular polarization, and the minus sign indicates left circular polarization. Performing this decomposition, we find that

$$\mathbf{E}_\omega^+ = \frac{1}{2} \begin{bmatrix} \cosh(kxx_0/z_R) - \sinh(kxx_0/z_R) \\ -i \cosh(kxx_0/z_R) + i \sinh(kxx_0/z_R) \end{bmatrix} \times 2Ae^{-k(x^2+y^2)/2z_R} e^{-kx_0^2/2z_R} \quad (32)$$

and

$$\mathbf{E}_\omega^- = \frac{1}{2} \begin{bmatrix} \cosh(kxx_0/z_R) + \sinh(kxx_0/z_R) \\ i \cosh(kxx_0/z_R) + i \sinh(kxx_0/z_R) \end{bmatrix} \times 2Ae^{-k(x^2+y^2)/2z_R} e^{-kx_0^2/2z_R} . \quad (33)$$

Thus, the amplitude of the left and right circularly polarized components are

$$E_\omega^+ = \frac{I}{2} [\cosh(kxx_0/z_R) - \sinh(kxx_0/z_R)] \times 2Ae^{-k(x^2+y^2)/2z_R} e^{-kx_0^2/2z_R} \quad (34)$$

and

$$\mathbf{E}_\omega^- = \frac{I}{2} \left[\cosh(kxx_0/z_R) + \sinh(kxx_0/z_R) \right] \times 2Ae^{-k(x^2+y^2)/2z_R} e^{-kx_0^2/2z_R}. \quad (35)$$

Substituting these in the equation for the third harmonic and simplifying, we obtain

$$\mathbf{E}_{3\omega}(x, y, x_0) \propto \begin{bmatrix} \cosh(kxx_0/z_R) \\ -i \sinh(kxx_0/z_R) \end{bmatrix} e^{-3k(x^2+y^2)/2z_R} e^{-3kx_0^2/2z_R}. \quad (36)$$

We want to find a measurement that is related to the spatial distribution of the focus in the x-y plane, so consider detecting the entire THG signal as a function of the beam separation x_0 . Calculating the intensity of third harmonic,

$$\begin{aligned} \mathbf{I}_{3\omega}(x, y, x_0) &\propto \mathbf{E}_{3\omega}(x, y, x_0) \cdot \mathbf{E}_{3\omega}^*(x, y, x_0) \\ &\propto \left[\cosh^2(kxx_0/z_R) + \sinh^2(kxx_0/z_R) \right] e^{-3k(x^2+y^2)/z_R} e^{-3kx_0^2/z_R} \end{aligned} \quad (37)$$

Now if we assume that we can detect all of the third harmonic signal and integrate over x and y,

$$\mathbf{I}_{3\omega}(x_0) \propto \int_{-\infty}^{\infty} \int_{-\infty}^{\infty} \mathbf{I}_{3\omega}(x, y, x_0) dx dy \quad (38)$$

Recognizing that the integral in y is a constant in x_0 , we find

$$\mathbf{I}_{3\omega}(x_0) \propto e^{-3kx_0^2/z_R} \int_{-\infty}^{\infty} e^{-3ky^2/z_R} dy \int_{-\infty}^{\infty} e^{-3kx^2/z_R} \left[\cosh^2(kxx_0/z_R) + \sinh^2(kxx_0/z_R) \right] dx \quad (39)$$

Performing the integration over x ,

$$I_{3\omega}(x_0) \propto e^{-8kx_0^2/3z_R} \quad (40)$$

Since it is frequently easier to move only one beam, the profile may be rewritten in terms of the separation between the beams $d = 2x_0$.

$$I_{3\omega}(d) \propto e^{-2kd^2/3z_R}. \quad (41)$$

Thus we see that the total THG produced by a two overlapping Gaussian beams of opposite circular polarization is Gaussian in the separation of the beams, d . In other words, a THG spatial correlation using identical Gaussian beams with opposite circular polarizations produces a background-free Gaussian profile, which can be used to characterize the spatial dimension of the focus in the xy -plane. One can show that the measured full width at half maximum of the THG spatial correlation as a function of beam separation, d_{FWHM} , is related to the full width at half of intensity profile of the beam, D_{FWHM} , by

$$d_{FWHM} = (3/2)^{1/2} D_{FWHM} \approx 1.224 D_{FWHM}. \quad (42)$$

Spatial characterization of a 0.65 NA focus

We have completely measured the spatial characteristics of a 0.65 NA beam using the THG signal. In Figure 8, the axial focus is characterized by scanning the coverslip through focus and measuring the THG signal as a function of axial displacement. For this measurement, the input beam is linearly polarized, and the THG signal is simply measured as a function of axial displacement through the focus. The calculated axial focus is $4.2 \mu\text{m}$ ($\text{FWHM}_{\text{axial}} \approx z_0 = 2n\lambda/(\text{NA})^2 \times 85\%$), and the measured value is $3.8 \mu\text{m}$. The calculated value is based on the traditional first node in the Bessel function and is given by z_0 , which is the normal metric used in microscopy for calculating the expected axial resolution. The FWHM is $\sim 85\%$ of this value. The agreement is excellent, considering that the input to the system is in fact a Gaussian beam.

In Figure 9, the lateral spatial profile is characterized by the background free spatial correlation technique outlined previously. Since the our focused beam is radially symmetric and the beams are circularly polarized, there is no preferred direction of the lateral scan, and scanning along a single dimension is sufficient to characterize the beam profile. Note the excellent fit to the shape Gaussian as described in the model. The measured lateral FWHM of the trace is $0.95 \mu\text{m}$. Again assuming a Bessel beam, the calculated value for the fundamental lateral focus is $0.85 \mu\text{m}$ ($\text{FWHM} = 0.61\lambda/\text{NA} \times 85\%$). Deconvolving the $0.92\text{-}\mu\text{m}$ measured FWHM of the trace using Equation 42, the deconvolved lateral FWHM is $0.77 \mu\text{m}$, in good agreement with the calculated value.

III. Collinear temporal autocorrelation using two beams of opposite circular polarization: CTHGx and CTHGy autocorrelation

Overlapping Opposite Circular Polarizations with a time delay

Ideally in any nonlinear imaging application it is desirable to know the pulse duration and spot size at the focus of the imaging optic. We can characterize the pulse duration at focus through a variety of interferometric techniques including two-photon absorption autocorrelations[12-14], third harmonic generation[5, 8, 15] or second harmonic generation[16]. Collinear techniques such as these are essential if the measurement is to be performed at the full NA of the objective. Here we introduce a new method that has the advantage over its predecessors in that it is background-free and can be done without the addition of a fluorophore [12] or special harmonic crystal [16]. As in [8, 15] all that is necessary for making this measurement is a typical glass coverslip.

We begin by numerically analyzing the third-order intensity autocorrelation function produced by circularly polarized beams, which is more complex than its predecessors based on plane polarization. From Equation 4, the third-harmonic field generated by two oppositely circularly polarized, overlapped beams with one delayed by a time τ , is given by the following expression

$$\mathbf{E}_{3\omega}(t, \tau) \propto \begin{bmatrix} I \\ -i \end{bmatrix} E_{\omega}^{+}(t)^2 E_{\omega}^{-}(t - \tau) + \begin{bmatrix} I \\ i \end{bmatrix} E_{\omega}^{+}(t) E_{\omega}^{-}(t - \tau)^2 \quad (43)$$

where the + and – indicate the polarization of the beams. Assuming the field amplitudes are equal, i.e. $E_{\omega}^{+}(t) = E_{\omega}^{-}(t) = E_{\omega}(t)$, then

$$\mathbf{E}_{3\omega}(t, \tau) \propto \begin{bmatrix} I \\ -i \end{bmatrix} E_{\omega}(t)^2 E_{\omega}(t - \tau) + \begin{bmatrix} I \\ i \end{bmatrix} E_{\omega}(t) E_{\omega}(t - \tau)^2 \quad (44)$$

We may now consider three obvious different autocorrelations: 1) detecting the x-component of the field, 2) detecting the y-component of the field, and 3) detecting the total field.

X-component

By placing a linear polarizer that is oriented to pass the x-component of the beam, we obtain

$$\mathbf{E}_{3\omega x}(t, \tau) \propto E_{\omega}^2(t)E_{\omega}(t - \tau) + E_{\omega}(t)E_{\omega}^2(t - \tau). \quad (45)$$

By varying the delay and detecting with a square law detector, we obtain what we call the CTHGx autocorrelation

$$I_x^{CTHG}(\tau) \propto \int_{-\infty}^{\infty} \left| E_{\omega}^2(t)E_{\omega}(t - \tau) + E_{\omega}(t)E_{\omega}^2(t - \tau) \right|^2 dt \quad (46)$$

This is essentially a background-free, interferometric autocorrelation as can be seen in Figure 10, which shows this autocorrelation as a function of delay.

Y-component

By placing a linear polarizer that is oriented to pass the y-component of the beam, we obtain

$$\mathbf{E}_{3\omega y}(t, \tau) \propto i \left(E_{\omega}^2(t)E_{\omega}(t - \tau) - E_{\omega}(t)E_{\omega}^2(t - \tau) \right). \quad (47)$$

By varying the delay and detecting with a square law detector, we obtain the CTHGy autocorrelation

$$I_y^{CTHG}(\tau) \propto \int_{-\infty}^{\infty} \left| E_{\omega}^2(t) E_{\omega}(t - \tau) - E_{\omega}(t) E_{\omega}^2(t - \tau) \right|^2 dt \quad (48)$$

This is essentially a background-free, interferometric autocorrelation that is π out of phase with the x-component autocorrelation as can be seen in Figure 11, which shows this autocorrelation as a function of delay.

Total field detection

If we detect both polarizations, then

$$\begin{aligned} |E_{3\omega}^{Total}|^2 &\propto \mathbf{E}_{3\omega}(t, \tau) \cdot \mathbf{E}_{3\omega}(t, \tau)^* \\ &\propto 2 \left[I_{\omega}^2(t) I_{\omega}(t - \tau) + I_{\omega}(t) I_{\omega}^2(t - \tau) \right] \end{aligned} \quad (49)$$

Thus, we obtain what we call the CTHG autocorrelation

$$I_{Total}^{CTHG}(\tau) \propto 2 \int_{-\infty}^{\infty} \left[I_{\omega}^2(t) I_{\omega}(t - \tau) + I_{\omega}(t) I_{\omega}^2(t - \tau) \right] dt \quad (50)$$

This is essentially a background-free, non-interferometric autocorrelation that is the envelope of the x-component and y-component autocorrelations, which we call the

CTHG autocorrelation . This can be seen in Figure 12, which shows this autocorrelation as a function of delay.

Collinear, background-free, non-interferometric autocorrelations

Figure 13 shows the measured, background free, THG autocorrelation. The spectrum of the pulse is also presented. The full width at half maximum of the spectrum measures 9.4 nm, and the pulsewidth is 157 fs (assuming a Gaussian) for a time bandwidth product of 0.4, indicating that the pulse is essentially transform limited at the focal plane of the microscope.

IV. Collinear THG FROG using two beams of opposite circular polarization: CTHG FROG

While we have shown that we can use polarization effects in the generation of THG to obtain measures of the focal parameters and temporal pulse width, full characterization of the pulse amplitude and phase may also be possible. Here we discuss using the delay dependent signal from the THG produced by two collinearly focused beams of equal magnitude and opposite circular polarization to produce a new collinear form of THG frequency-resolved optical gating (FROG)[17], which we will call CTHG FROG. The advantage of this method is that since the individual beams are circularly polarized, the THG signal is generated only when the pulses overlap temporally, which means that CTHG FROG is a collinear method, which can thus be used for beams with the full NA in a microscope that is inherently background-free. To date, only one other collinear, background free FROG exists[16], and it requires placing a second harmonic crystal at the focus. CTHG FROG, on the other hand, could use the coverslip as the nonlinear medium as was done for the autocorrelation in Section V.

For all forms of FROG, the signal is the magnitude squared of the Fourier transform of the signal field (i.e. the magnitude squared of the spectrum of the autocorrelation field), or

$$I_{FROG}(\omega, \tau) = \left| \int_{-\infty}^{\infty} E_{sig}(t, \tau) e^{-i\omega t} dt \right|^2. \quad (51)$$

Thus for CTHG FROG, we need to deal explicitly with the vector nature of the field

$$\mathbf{E}_{sig}^{CTHG}(t, \tau) = E(t)E(t - \tau) \begin{bmatrix} E(t) + E(t - \tau) \\ i(E(t) - E(t - \tau)) \end{bmatrix}. \quad (52)$$

Thus, let us rewrite the FROG signal as

$$\begin{aligned} I_{FROG}(\omega, \tau) &= \int_{-\infty}^{\infty} \mathbf{E}_{sig}(t, \tau) e^{-i\omega t} dt \cdot \left[\int_{-\infty}^{\infty} \mathbf{E}_{sig}(t', \tau) e^{-i\omega t'} dt' \right]^* \\ &= \int_{-\infty}^{\infty} \int_{-\infty}^{\infty} \mathbf{E}_{sig}(t, \tau) \cdot \mathbf{E}_{sig}^*(t', \tau) e^{-i\omega t} e^{i\omega t'} dt dt' \end{aligned} \quad (53)$$

Substituting the form of the total signal field for THG in, the FROG signal becomes

$$\begin{aligned} I_{FROG}^{CTHG}(\omega, \tau) &= \int_{-\infty}^{\infty} \int_{-\infty}^{\infty} E(t)E(t - \tau) \begin{bmatrix} E(t) + E(t - \tau) \\ i(E(t) - E(t - \tau)) \end{bmatrix} \\ &\quad E^*(t')E^*(t' - \tau) \begin{bmatrix} E^*(t') + E^*(t' - \tau) \\ -i(E^*(t') - E^*(t' - \tau)) \end{bmatrix} e^{-i\omega t} e^{i\omega t'} dt dt' \end{aligned} \quad (54)$$

Performing the vector multiplication,

$$\begin{aligned}
I_{FROG}^{CTHG}(\omega, \tau) = & 2 \int_{-\infty}^{\infty} \int_{-\infty}^{\infty} E^2(t) E(t - \tau) E^{*2}(t') E^*(t' - \tau) \\
& + E(t) E^2(t - \tau) E^*(t') E^{*2}(t' - \tau) e^{-i\omega t} e^{i\omega t'} dt dt'
\end{aligned} \tag{55}$$

Separating out the integrals, we find

$$I_{FROG}^{CTHG}(\omega, \tau) = 2 \left| \int_{-\infty}^{\infty} E^2(t) E(t - \tau) e^{-i\omega t} dt \right|^2 + 2 \left| \int_{-\infty}^{\infty} E(t) E^2(t - \tau) e^{-i\omega t} dt \right|^2, \tag{56}$$

and we can see that the CTHG FROG signal is essentially the sum of the two possible noncollinear THG FROG traces.

The form of Equation 56 is not the standard form that is used for phase retrieval in FROG, and while it may be possible to alter the algorithms that are currently used for to retrieve the field from FROG traces to retrieve the field from this form, the difficulty of measuring the spectrum properly in two polarizations at once makes it experimentally simpler to place a polarizer in before the spectrometer to separate out either the x or y component of the field. Thus using only the x-component of the THG, we obtain the CTHGx FROG signal

$$I_{FROG}^{CTHGx}(\omega, \tau) = \left| \int_{-\infty}^{\infty} (E^2(t) E(t - \tau) + E(t) E^2(t - \tau)) e^{-i\omega t} dt \right|^2, \tag{57}$$

and using only the y-component of the THG, we obtain the CTHGy FROG signal

$$I_{FROG}^{CTHGy}(\omega, \tau) = \left| \int_{-\infty}^{\infty} (E^2(t)E(t-\tau) - E(t)E^2(t-\tau))e^{-i\omega t} dt \right|^2. \quad (58)$$

These are just the frequency-resolved forms of the CTHGx and CTHGy autocorrelations that were derived in Section III. Figure 14 shows a theoretical the CTHGx FROG trace for a 5-fs Gaussian pulse. The trace is background free, but it is fringe-resolved, which greatly increases the amount of data that is required relative to a more typical non-fringe resolved FROG trace, especially for pulses that are many cycles long. The CTHGy FROG trace is similar to the CTHGx FROG trace except with the fringes 180° out of phase just as occurs in the Figures 10 and 11 for the CTHGx and CTHGy autocorrelations.

We have written a generalized-projection code for the retrieval of the CTHGx traces. For the readers' convenience, the mathematical forms of the generalized projections for phase retrieval from traces of these forms are derived in the Appendix. While we are able to retrieve some theoretical traces to the numerical accuracy of the machine, we are currently experiencing problems with stagnation of the algorithm even for traces of simple pulses that are only a few cycles long. This may be due to the difficulty of required explicit handling the high-frequency component of the electric field, which is not required in the non-fringe resolved traces for which FROG is know to work well. Since we have had difficulty with the retrieval for the similar but even more difficult problem of interferometric second-harmonic generation (ISHG) FROG, which is also fringe-resolved, but not background free, we cannot recommend attempting fringe-

resolved FROG measurements at this time. We do believe, however, that improved algorithms may yet make such measurements useful for actual retrieval. We also note that experimentally the FROG trace is itself an accurate representation of the pulse and thus the CTHG, CTHG_x or CTHG_y FROG traces may be of significant value for characterizing the pulse at the focus of high-NA objectives even without a full retrieval of the field and phase.

V. Summary & Conclusions

In this work, we have investigated the polarization dependence of the THG process under tight focusing conditions. Specifically, we have shown that, even under tight focusing conditions, a simple plane wave analysis of the signal can be used to predict the polarization dependence of third-harmonic generated in a focus as a function of the polarization state of the incident beam. This is significant in that ellipticity is an additional parameter that might be exploited to provide image contrast, and these measurements enable a quantitative measure of these image intensities in a very simple way. Exploiting the fact that we could use the plane wave analysis, we then showed that circularly polarized beams can be used to quantitatively characterize the lateral dependence of the spatial focus of high NA systems, which can be combined with a measurement of the axial dependence using a linear polarization for a complete spatial characterization of the spatial focus .

We have also used our new understanding of the plane wave character of the generation at the focus to make novel collinear, background-free, third-harmonic intensity autocorrelations of the pulse at the focus. This is significant because prior to this work there has been no single tool that provided background free spatio-temporal

characterization of focal volumes such as those used in high-resolution microscopy. We also discuss the possibility of using third harmonic generation with circularly polarized beams for background-free collinear frequency resolved optical gating.

VI. Acknowledgements

This work was partially supported by the National Institute of Health under grant R21 EB001722-01. This work was performed under the auspices of the U.S. Department of Energy by University of California, Lawrence Livermore National Laboratory under Contract W-7405-Eng-48.

VII. Appendix—Generalized Projections for CTHG FROG

Here we will follow the notation of Trebino[17] and derive the generalized projections that are for used the phase retrieval for the FROG traces obtained using either the x- or y-component of the signal field. In the generalized projections method of phase retrieval, we minimize the functional distance

$$Z = \sum_{i,j=1}^N \left| E_{sig}^{(k)}(t_i, \tau_j) - E_{sig}^{(k+1)}(t_i, \tau_j) \right|^2 \quad (A1)$$

where the summation in i and j indicate the individual axes in the NxN FROG traces and k is the iteration of the FROG algorithm.

X-component

To do this, we explicitly substitute the mathematical form of the nonlinearity, so for the x-component of the CTHG signal

$$Z^{CTHGx} = \sum_{i,j=l}^N \left| E_{sig}^{(k)}(t_i, \tau_j) - [E^{(k+l)}(t_i)]^2 E^{(k+l)}(t_i - \tau_j) - E^{(k+l)}(t_i) [E^{(k+l)}(t_i - \tau_j)] \right|^2. \quad (A2)$$

To actually perform the functional minimization, we must calculate

$$\frac{\partial Z^{CTHGx}}{\partial \text{Re}\{E(t_k)\}} \text{ and } \frac{\partial Z^{CTHGx}}{\partial \text{Im}\{E(t_k)\}}. \quad (A3)$$

For convenience let

$$\sigma^{CTHGx} = E_{sig}(t_i, \tau_j) - E^2(t_i)E(t_i - \tau_j) - E(t_i)E^2(t_i - \tau_j). \quad (A4)$$

As in [17]I have dropped the k superscripts to simplify the equations that result.

$E_{sig}(t_i, \tau_j)$ always indicates the k^{th} iteration of the signal field, and $E(t_i)$ always indicates the $k+l^{\text{st}}$ iteration for the pulse field. Thus we can calculate the derivatives as follows.

$$\begin{aligned}
\frac{\partial Z^{CTHGx}}{\partial \text{Re}\{E(t_k)\}} &= \frac{\partial}{\partial \text{Re}\{E(t_k)\}} \sum_{i,j=1}^N |\sigma^{CTHGx}|^2 \\
&= \sum_{i,j=1}^N \frac{\partial}{\partial \text{Re}\{E(t_k)\}} |\sigma^{CTHGx}|^2 \\
&= \sum_{i,j=1}^N \frac{\partial}{\partial \text{Re}\{E(t_k)\}} \sigma^{CTHGx} (\sigma^{CTHGx})^* \\
&= \sum_{i,j=1}^N \left[\frac{\partial \sigma^{CTHGx}}{\partial \text{Re}\{E(t_k)\}} \right] (\sigma^{CTHGx})^* + c.c.
\end{aligned} \tag{A5}$$

Substituting in for σ^{CTHGx} , we obtain

$$\begin{aligned}
\frac{\partial Z^{CTHGx}}{\partial \text{Re}\{E(t_k)\}} &= \sum_{i,j=1}^N \left[\frac{\partial}{\partial \text{Re}\{E(t_k)\}} \left(E_{sig}(t_i, \tau_j) - E^2(t_i)E(t_i - \tau_j) - E(t_i)E^2(t_i - \tau_j) \right) \right] (\sigma^{CTHGx})^* + c.c. \\
&= \sum_{i,j=1}^N \left[-2E(t_i)E(t_i - \tau_j) \frac{\partial E(t_i)}{\partial \text{Re}\{E(t_k)\}} - E^2(t_i) \frac{\partial E(t_i - \tau_j)}{\partial \text{Re}\{E(t_k)\}} \right. \\
&\quad \left. - 2E(t_i)E(t_i - \tau_j) \frac{\partial E(t_i - \tau_j)}{\partial \text{Re}\{E(t_k)\}} - E^2(t_i - \tau_j) \frac{\partial E(t_i)}{\partial \text{Re}\{E(t_k)\}} \right] (\sigma^{CTHGx})^* + c.c.
\end{aligned} \tag{A6}$$

Using the following identities

$$\frac{\partial E(t_i)}{\partial \text{Re}\{E(t_k)\}} = \delta(t_i - t_k) \quad (\text{A7})$$

$$\frac{\partial E(t_i - \tau_j)}{\partial \text{Re}\{E(t_k)\}} = \delta(t_i - \tau_j - t_k)$$

we obtain

$$\begin{aligned} \frac{\partial Z^{CTHGx}}{\partial \text{Re}\{E(t_k)\}} &= \sum_{i,j=1}^N \left[-2E(t_i)E(t_i - \tau_j)\delta(t_i - t_k) - E^2(t_i)\delta(t_i - \tau_j - t_k) \right. \\ &\quad \left. - 2E(t_i)E(t_i - \tau_j)\delta(t_i - \tau_j - t_k) - E^2(t_i - \tau_j)\delta(t_i - t_k) \right] (\sigma^{CTHGx})^* + c.c. \\ &= \sum_{i,j=1}^N \left[-[2E(t_i)E(t_i - \tau_j) + E^2(t_i - \tau_j)]\delta(t_i - t_k) (\sigma^{CTHGx})^* \right. \\ &\quad \left. + \sum_{i,j=1}^N -[2E(t_i)E(t_i - \tau_j) + E^2(t_i)]\delta(t_i - \tau_j - t_k) \right] (\sigma^{CTHGx})^* + c.c. \end{aligned} \quad (\text{A8})$$

Explicitly using the delta functions to eliminate the summations over i ,

$$\begin{aligned}
\frac{\partial Z^{CTHGx}}{\partial \text{Re}\{E(t_k)\}} &= \sum_{j=1}^N \left[-\left[2E(t_k)E(t_k - \tau_j) + E^2(t_k - \tau_j) \right] \right. \\
&\quad \times \left[E_{sig}^*(t_k, \tau_j) - E^{*2}(t_k)E^*(t_k - \tau_j) - E^*(t_k)E^{*2}(t_k - \tau_j) \right] \\
&\quad + \sum_{j=1}^N \left[-\left[2E(t_k + \tau_j)E(t_k) + E^2(t_k + \tau_j) \right] \right. \\
&\quad \times \left[E_{sig}^*(t_k + \tau_j, \tau_j) - E^{*2}(t_k + \tau_j)E^*(t_k) - E^*(t_k + \tau_j)E^{*2}(t_k) \right] \left. \right] + c.c.
\end{aligned} \tag{A9}$$

$$\begin{aligned}
\frac{\partial Z^{CTHGx}}{\partial \text{Re}\{E(t_k)\}} &= \sum_{j=1}^N \left[\left[-2E(t_k)E(t_k - \tau_j) - E^2(t_k - \tau_j) \right] \right. \\
&\quad \times \left[E_{sig}^*(t_k, \tau_j) - E^{*2}(t_k)E^*(t_k - \tau_j) - E^*(t_k)E^{*2}(t_k - \tau_j) \right] \\
&\quad + \left[-2E(t_k + \tau_j)E(t_k) - E^2(t_k + \tau_j) \right] \\
&\quad \times \left[E_{sig}^*(t_k + \tau_j, \tau_j) - E^{*2}(t_k + \tau_j)E^*(t_k) - E^*(t_k + \tau_j)E^{*2}(t_k) \right] \left. \right] \\
&\quad + c.c.
\end{aligned} \tag{A10}$$

We may calculate the other derivative, similarly by starting with

$$\frac{\partial Z^{CTHGx}}{\partial \text{Im}\{E(t_k)\}} = \frac{\partial}{\partial \text{Im}\{E(t_k)\}} \sum_{i,j=1}^N \left| \sigma^{CTHGx} \right|^2, \tag{A11}$$

and using the following identities

$$\frac{\partial E(t_i)}{\partial \text{Im}\{E(t_k)\}} = i\delta(t_i - t_k)$$

$$\frac{\partial E(t_i - \tau_j)}{\partial \text{Im}\{E(t_k)\}} = i\delta(t_i - \tau_j - t_k)$$
(A12)

We obtain

$$\begin{aligned} \frac{\partial Z^{CTHGx}}{\partial \text{Im}\{E(t_k)\}} = & i \sum_{j=1}^N \left[\left[-2E(t_k)E(t_k - \tau_j) - E^2(t_k - \tau_j) \right] \right. \\ & \times \left[E_{sig}^*(t_k, \tau_j) - E^{*2}(t_k)E^*(t_k - \tau_j) - E^*(t_k)E^{*2}(t_k - \tau_j) \right] \\ & + \left[-2E(t_k + \tau_j)E(t_k) - E^2(t_k + \tau_j) \right] \\ & \times \left[E_{sig}^*(t_k + \tau_j, \tau_j) - E^{*2}(t_k + \tau_j)E^*(t_k) - E^*(t_k + \tau_j)E^{*2}(t_k) \right] \Big] \\ & + c.c. \end{aligned}$$
(A13)

Y-component

Putting a polarizer in the THG output to pass only the y-component of the THG, the FROG signal becomes

$$I_{FROG}^{CTHGY}(\omega, \tau) = \left| \int_{-\infty}^{\infty} \left(E^2(t)E(t - \tau) - E(t)E^2(t - \tau) \right) e^{-i\omega t} dt \right|^2.$$
(A14)

The y-component of the CTHG signal is then

$$Z^{CTHGY} = \sum_{i,j=1}^N \left| E_{sig}^{(k)}(t_i, \tau_j) - [E^{(k+1)}(t_i)]^2 E^{(k+1)}(t_i - \tau_j) + E^{(k+1)}(t_i) [E^{(k+1)}(t_i - \tau_j)] \right|^2. \quad (A15)$$

To actually perform the functional minimization, we must calculate

$$\frac{\partial Z^{CTHGY}}{\partial \text{Re}\{E(t_k)\}} \text{ and } \frac{\partial Z^{CTHGY}}{\partial \text{Im}\{E(t_k)\}}. \quad (A16)$$

Solving as was done for the x-component

$$\begin{aligned} \frac{\partial Z^{CTHGY}}{\partial \text{Re}\{E(t_k)\}} &= \sum_{j=1}^N \left[[-2E(t_k)E(t_k - \tau_j) + E^2(t_k - \tau_j)] \right. \\ &\quad \times [E_{sig}^*(t_k, \tau_j) - E^{*2}(t_k)E^*(t_k - \tau_j) + E^*(t_k)E^{*2}(t_k - \tau_j)] \\ &\quad + [2E(t_k + \tau_j)E(t_k) - E^2(t_k + \tau_j)] \\ &\quad \times [E_{sig}^*(t_k + \tau_j, \tau_j) - E^{*2}(t_k + \tau_j)E^*(t_k) + E^*(t_k + \tau_j)E^{*2}(t_k)] \Big] \\ &\quad + c.c. \end{aligned} \quad (A17)$$

and

$$\begin{aligned}
\frac{\partial Z^{CTHGy}}{\partial \text{Im}\{E(t_k)\}} &= i \sum_{j=1}^N \left[\left[-2E(t_k)E(t_k - \tau_j) + E^2(t_k - \tau_j) \right] \right. \\
&\quad \times \left[E_{sig}^*(t_k, \tau_j) - E^{*2}(t_k)E^*(t_k - \tau_j) + E^*(t_k)E^{*2}(t_k - \tau_j) \right] \\
&\quad + \left[2E(t_k + \tau_j)E(t_k) - E^2(t_k + \tau_j) \right] \\
&\quad \times \left[E_{sig}^*(t_k + \tau_j, \tau_j) - E^{*2}(t_k + \tau_j)E^*(t_k) + E^*(t_k + \tau_j)E^{*2}(t_k) \right] \Big] \\
&\quad + c.c.
\end{aligned}
\tag{A18}$$

References

- [1] W. Denk, J. H. Strickler, and W. W. Webb, "Two-photon laser scanning fluorescence microscopy," *Science*, vol. 248, pp. 73-6, 1990.
- [2] G. H. Patterson and D. W. Piston, "Photobleaching in two-photon excitation microscopy," *Biophysical Journal*, vol. 78, pp. 2159-62, 2000.
- [3] J. F. Ward and G. H. C. New, "Optical third harmonic generation in gases by a focused laser beam," *Physical Review*, vol. 185, pp. 57-72, 1969.
- [4] T. Y. F. Tsang, "Optical third-harmonic generation at interfaces," *Physical Review A (Atomic, Molecular, and Optical Physics)*, vol. 52, pp. 4116-25, 1995.
- [5] Y. Barad, H. Eisenberg, M. Horowitz, and Y. Silberberg, "Nonlinear scanning laser microscopy by third-harmonic generation," *Applied Physics Letters*, vol. 70, pp. 922-924, 1997.
- [6] M. Müller, J. Squier, K. R. Wilson, and G. J. Brakenhoff, "3D-microscopy of transparent objects using third-harmonic generation," *Journal of Microscopy*, vol. 191, pp. 266-274, 1998.
- [7] T. Tsang, M. A. Krumbugel, K. W. DeLong, D. N. Fittinghoff, and R. Trebino, "Frequency-resolved optical-gating measurements of ultrashort pulses using surface third-harmonic generation," *Optics Letters*, vol. 21, pp. 1381-3, 1996.
- [8] D. Meshulach, Y. Barad, and Y. Silberberg, "Measurement of ultrashort optical pulses by third-harmonic generation," *Journal of the Optical Society of America B (Optical Physics)*, vol. 14, pp. 2122-5, 1997.
- [9] P. P. Bey and H. Rabin, "Coupled-Wave Solution of Harmonic Generation in an Optically Active Medium," *Physical Review*, vol. 162, pp. 794-800, 1967.

- [10] D. Kopf, F. X. Kartner, U. Keller, and K. J. Weingarten, "Diode-pumped mode-locked Nd:glass lasers with an antiresonant Fabry-Perot saturable absorber," *Optics Letters*, vol. 20, pp. 1169-71, 1995.
- [11] J. Squier and M. Muller, "High resolution nonlinear microscopy: A review of sources and methods for achieving optimal imaging," *Review of Scientific Instruments*, vol. 72, pp. 2855-67, 2001.
- [12] M. Muller, J. Squier, and G. J. Brakenhoff, "Measurement of femtosecond pulses in the focal point of a high-numerical-aperture lens by two-photon absorption," *Optics Letters*, vol. 20, pp. 1038-40, 1995.
- [13] A. C. Millard, D. N. Fittinghoff, J. A. Squier, M. Muller, and A. L. Gaeta, "Using GaAsP photodiodes to characterize ultrashort pulses under high numerical aperture focusing in microscopy," *Journal of Microscopy*, vol. 193, pp. 179-81, 1999.
- [14] T. Jasapara and W. Rudolph, "Characterization of sub-10-fs pulse focusing with high-numerical-aperture microscope objectives," *Optics Letters*, vol. 24, pp. 777-9, 1999.
- [15] J. A. Squier, D. N. Fittinghoff, C. P. J. Barty, K. R. Wilson, M. Muller, and G. J. Brakenhoff, "Characterization of femtosecond pulses focused with high numerical aperture optics using interferometric surface-third-harmonic generation," *Optics Communications*, vol. 147, pp. 153-6, 1998.
- [16] D. N. Fittinghoff, A. C. Millard, J. A. Squier, and M. Muller, "Frequency-resolved optical gating measurement of ultrashort pulses passing through a high

- numerical aperture objective," *IEEE Journal of Quantum Electronics*, vol. 35, pp. 479-86, 1999.
- [17] R. Trebino, K. W. DeLong, D. N. Fittinghoff, J. N. Sweetser, M. A. Krumbugel, B. A. Richman, and D. J. Kane, "Measuring ultrashort laser pulses in the time-frequency domain using frequency-resolved optical gating.," *Reviews of Scientific Instruments*, vol. 68, pp. 3277-95, 1997.

Figure Captions

- Figure 1 Polarization ellipse to show definitions of ellipticity and rotation angles.
- Figure 2 The x- and y-components of the third-harmonic field as functions of the ratio of the right- and left-circularly polarized amplitudes of the fundamental field.
- Figure 3 The magnitude and ellipticity angle of the third-harmonic field as functions of the ratio of the right- and left-circularly polarized amplitudes of the fundamental field.
- Figure 4 The diode-pumped Nd:glass (phosphate) laser used for the harmonic generation microscope in Figure 7. The average output power is 100 mW, the pulse duration is 150 fs, and the repetition rate is 100 MHz.
- Figure 5 The home-built microscope used for THG measurements in this Article. Optical signals at both the second and third harmonic are captured in the forward direction. In the back direction, multiphoton absorption fluorescence signals are measured. In this way images created through the three different techniques are fully registered with respect to each other.
- Figure 6 The measured and fit THG signals for generation using a 0.65 NA objective to focus at the surface of a coverslip.
- Figure 7 The measured and fit THG signals for generation using a 1.4 NA objective to focus at the surface of a coverslip.
- Figure 8 The THG signal as a function of axial displacement obtained by scanning the coverslip through focus. The calculated axial focus is $4.3 \mu\text{m}$ ($\text{FWHM} = 2n\lambda/(\text{NA})^2 \times 85\%$), and the measured value is $3.8 \mu\text{m}$.

Figure 9 The lateral spatial profile as characterized by the background free spatial THG correlation technique. Note the excellent fit to a Gaussian as described in the model. The calculated value for the fundamental lateral focus is $0.85 \mu\text{m}$ ($\text{FWHM} = .61\lambda/\text{NA} \times 85\%$). Deconvolving the $0.92\text{-}\mu\text{m}$ measured FWHM of the trace using Equation 42, the deconvolved lateral FWHM is $0.77 \mu\text{m}$, in good agreement with the calculated value.

Figure 10 The x-component CTHG autocorrelation of a 15-fs, transform limited Gaussian pulse with a center wavelength of 800 nm.

Figure 11 The y-component CTHG autocorrelation of a 15-fs, transform limited Gaussian pulse with a center wavelength of 800 nm.

Figure 12 The total-field CTHG autocorrelation of a 15-fs, transform limited Gaussian pulse with a center wavelength of 800 nm.

Figure 13 The measured, background free, THG autocorrelation. The spectrum of the pulse is also presented. The full width at have maximum of the spectrum measures 9.4 nm, and the pulsewidth 157 fs (assuming a Gaussian) for a time bandwidth product of 0.4, indicating that the pulse is essentially transform limited at the focal plane of the microscope.

Figure 14 Calculated background free, collinear FROG trace.

Figures

Figure 1

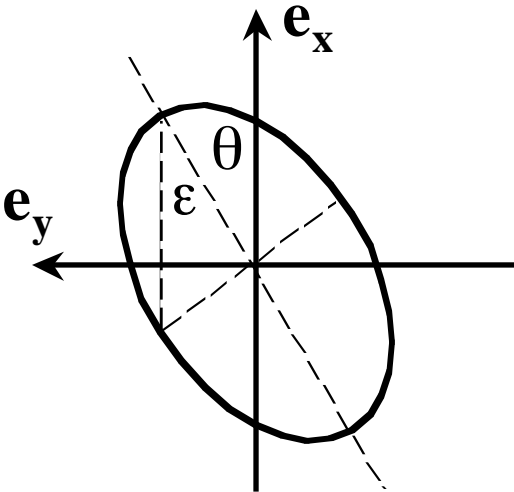


Figure 2

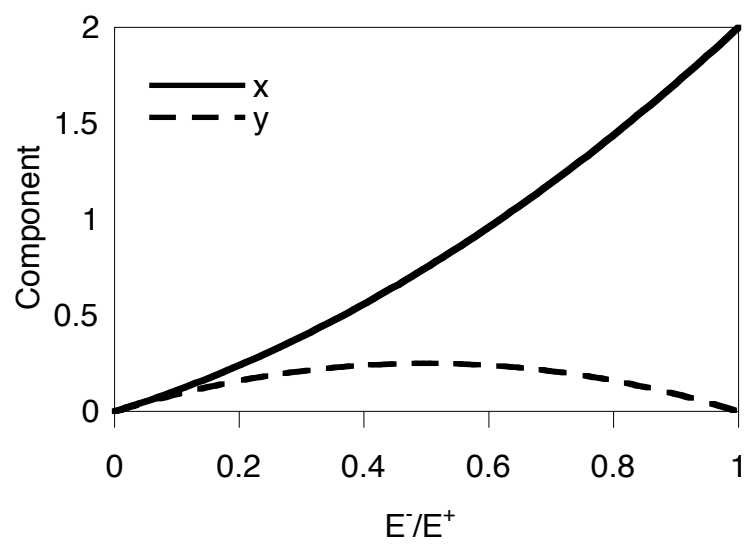


Figure 3

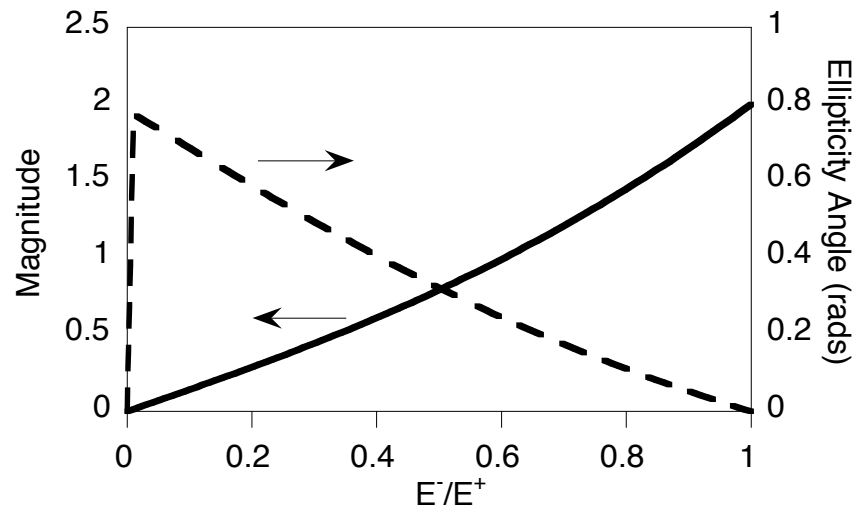


Figure 4

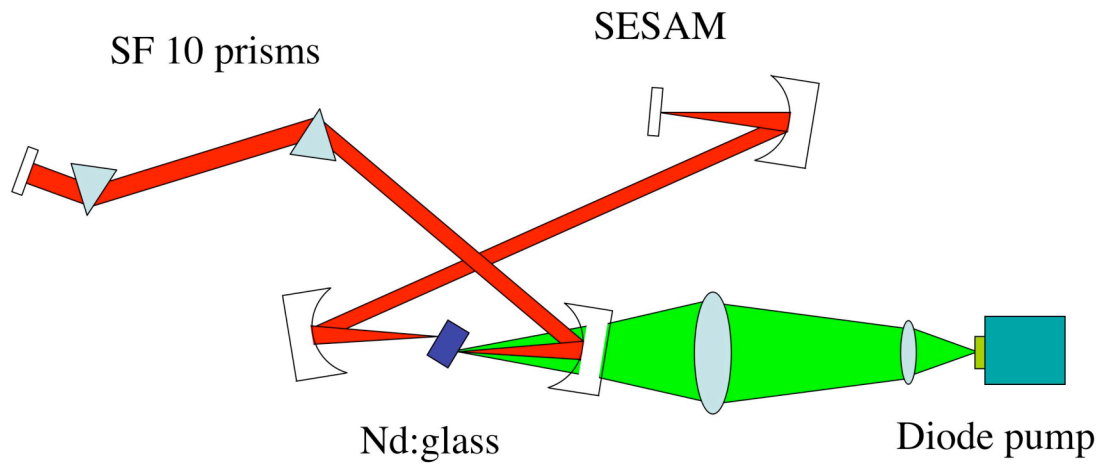


Figure 5

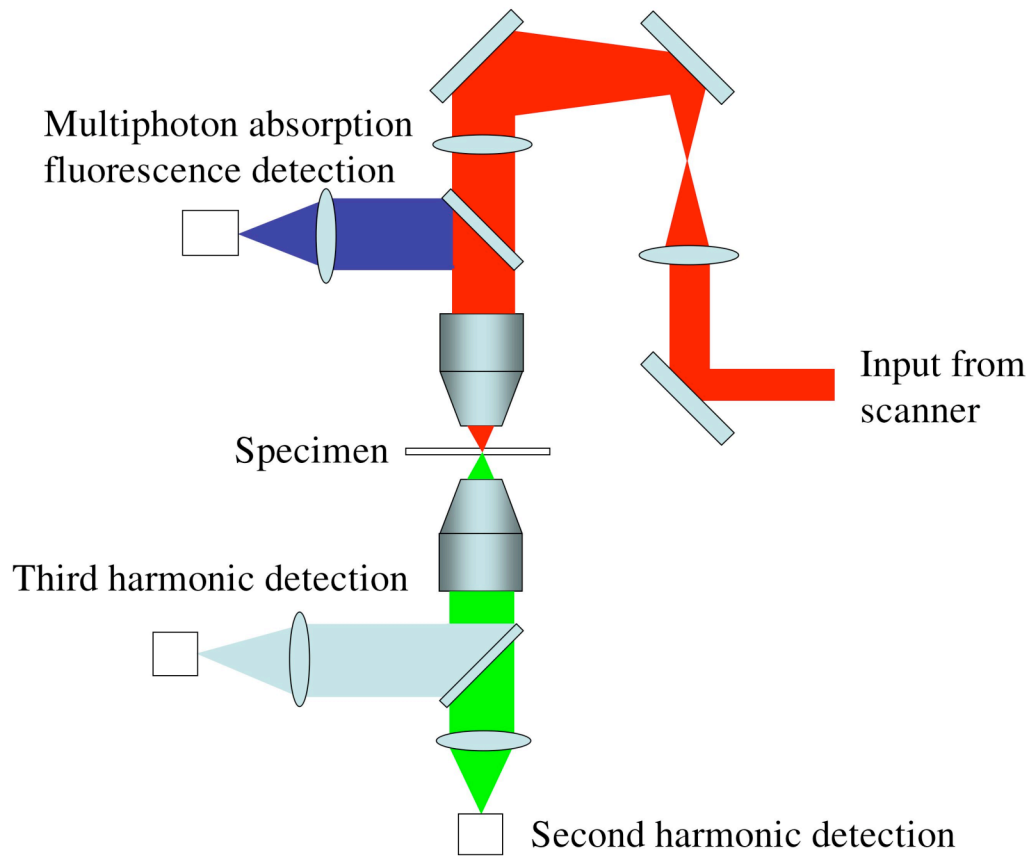


Figure 6

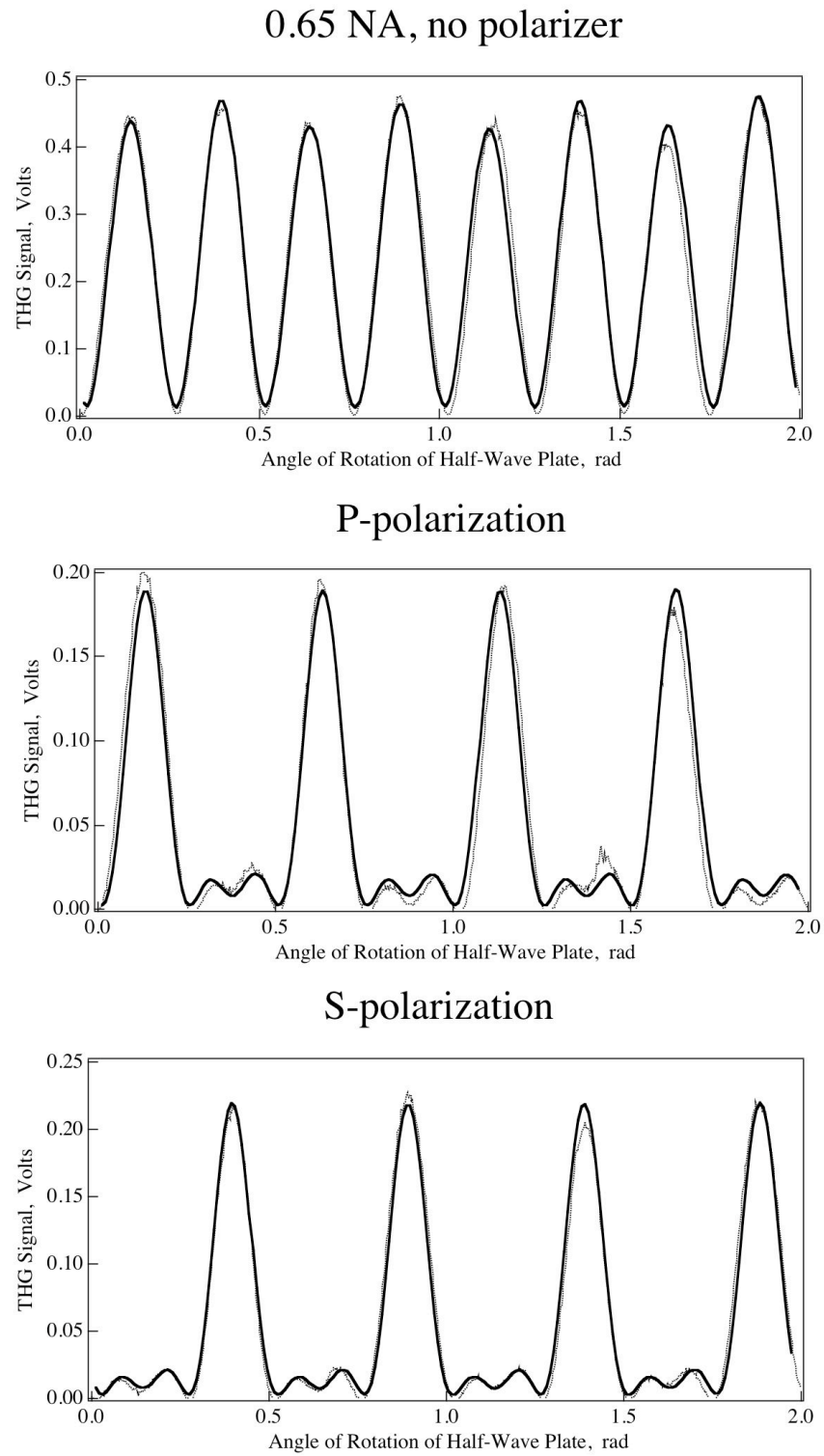


Figure 7

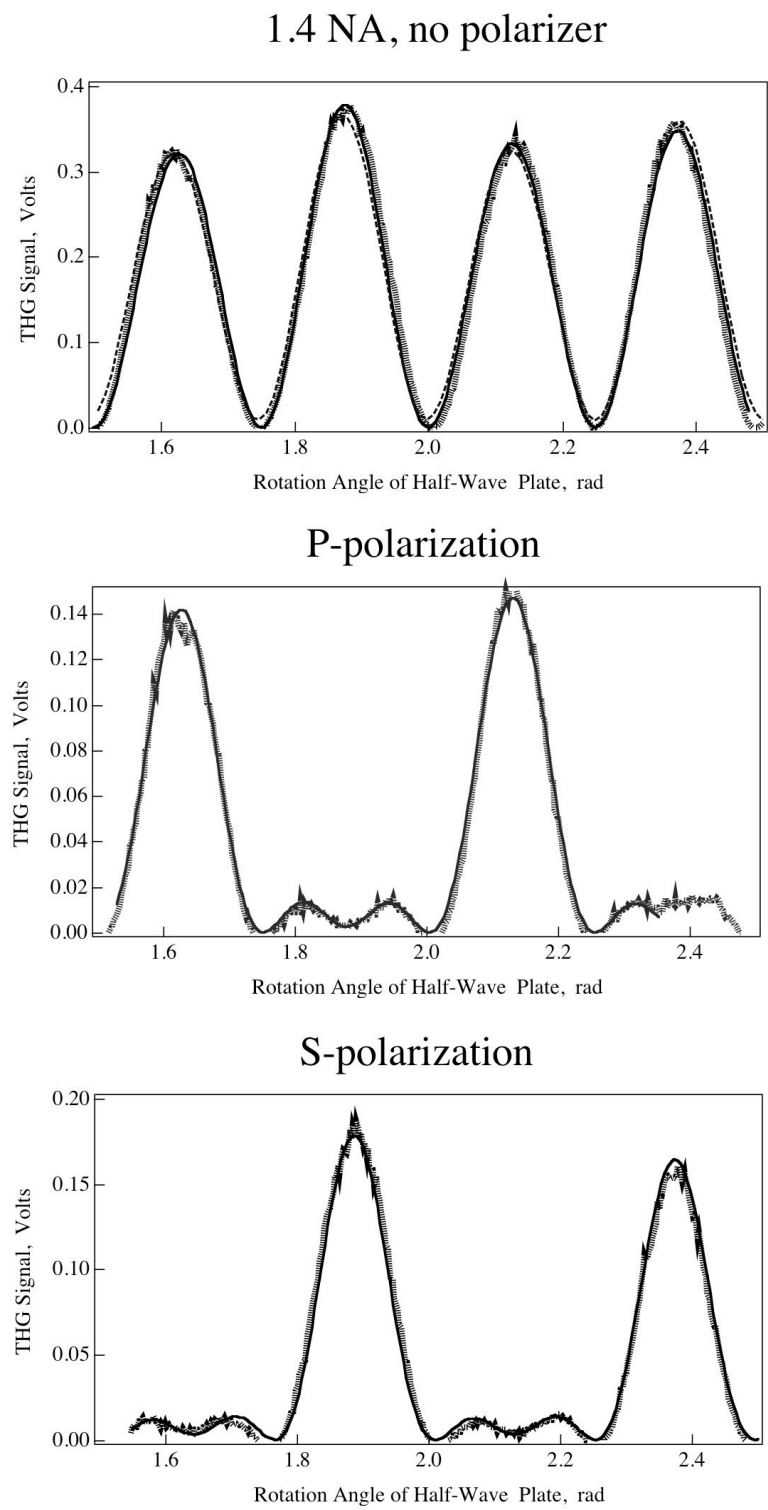


Figure 8

Axial beam size measurement

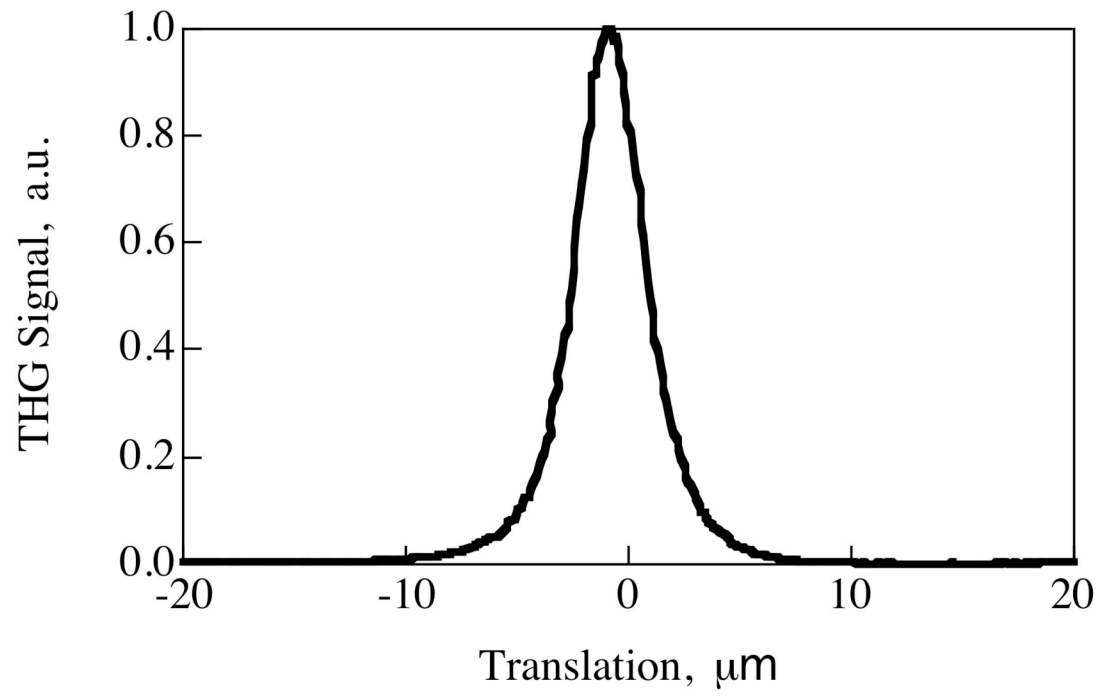


Figure 9

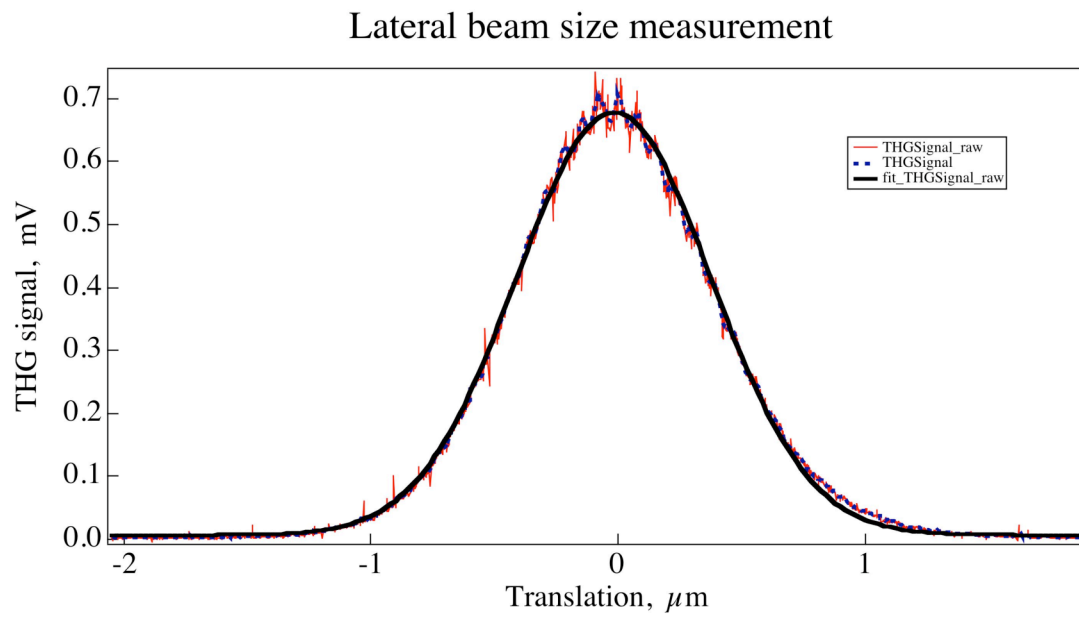


Figure 10

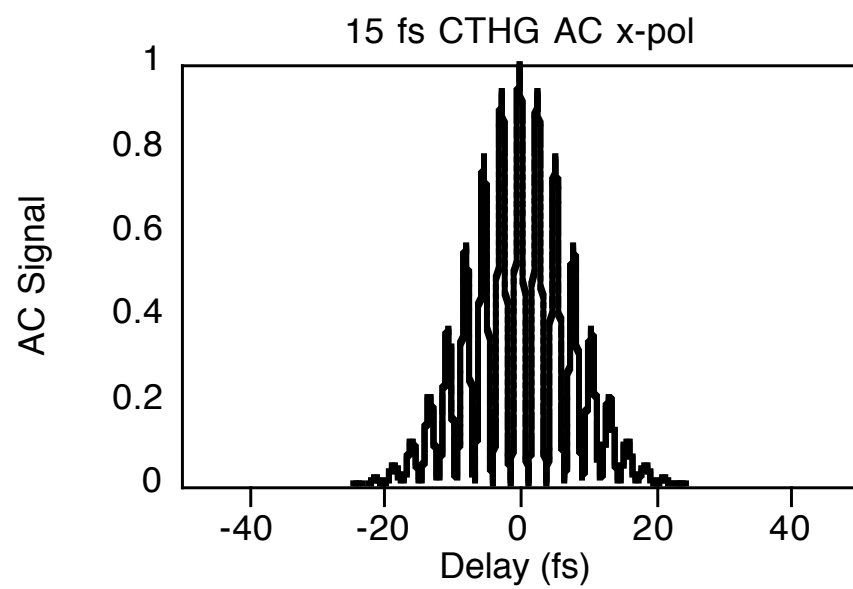


Figure 11

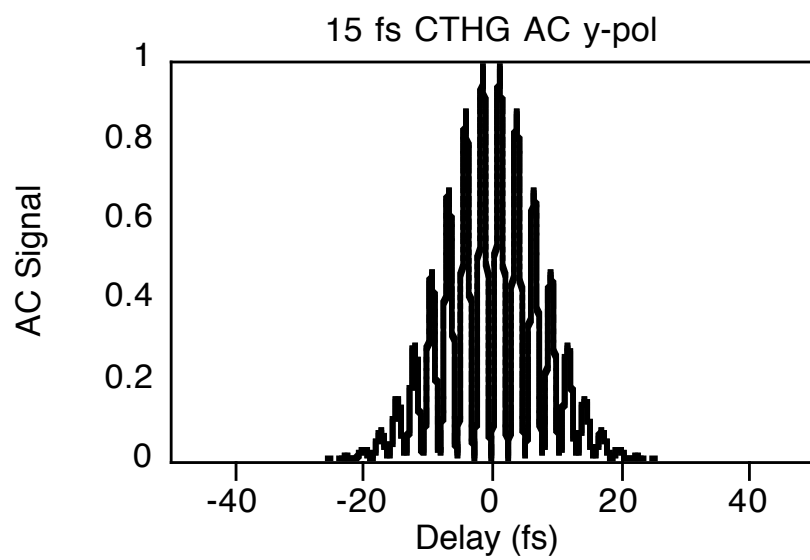


Figure 12

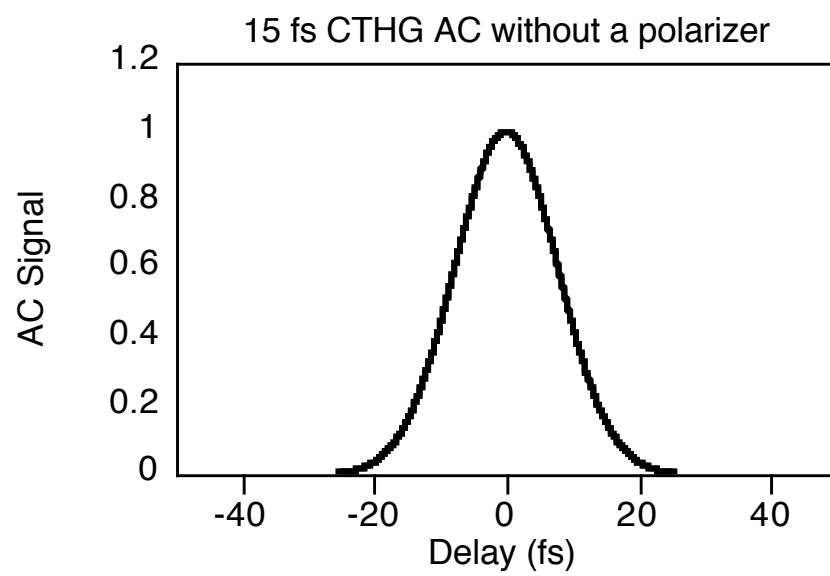


Figure 13

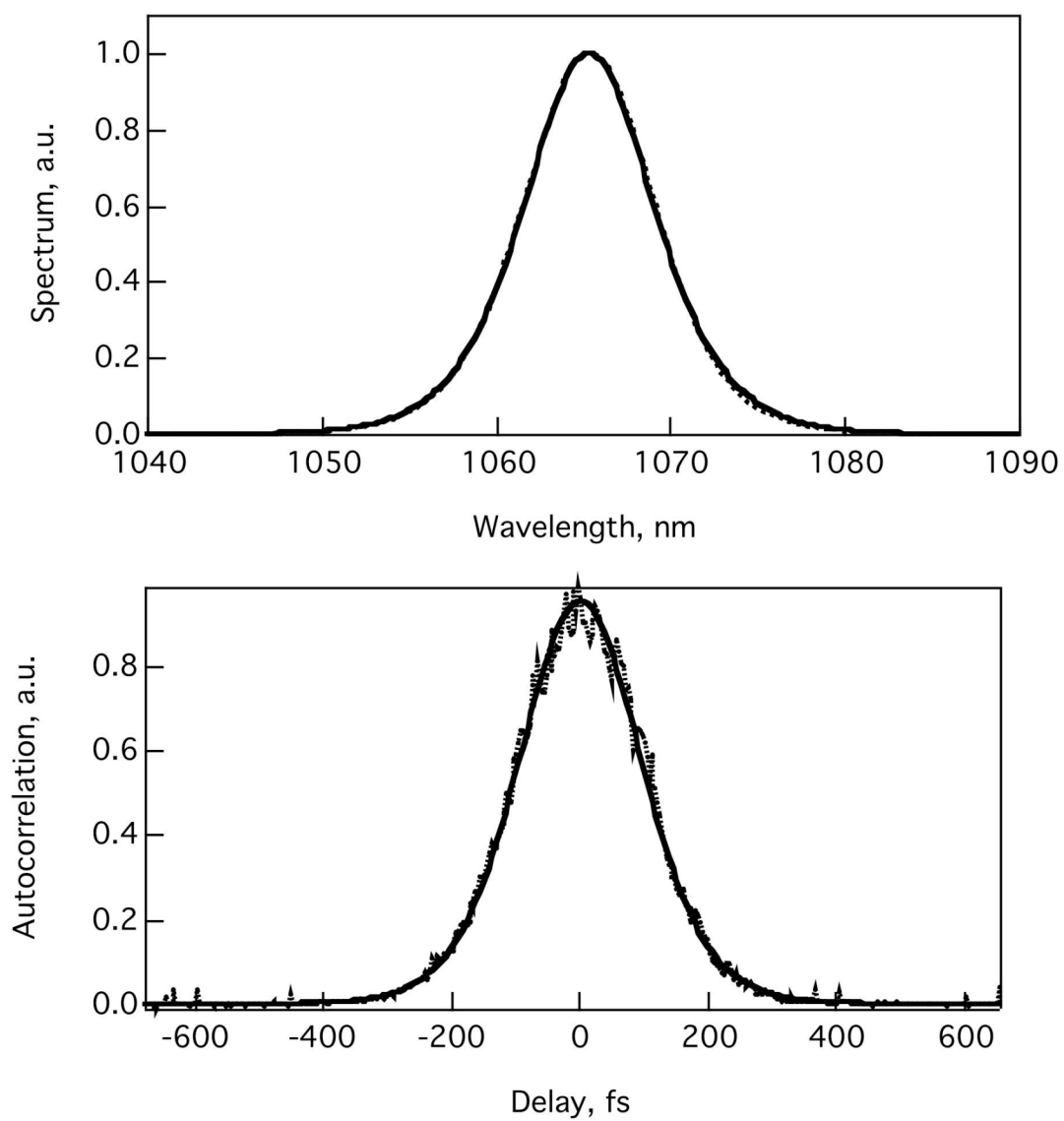


Figure 14

